

POST-PROCESSING THICKNESS VARIATION OF PV MODULE MATERIALS AND ITS IMPACT ON TEMPERATURE, MECHANICAL STRESS AND POWER

Andrea Pfreundt, Andreas J. Beinert, Damla Yucebas, Laila Verissimo Mesquita, Luciana Pitta-Bauermann, Pascal Romer, Max Mittag

Fraunhofer Institute for Solar Energy Systems ISE,
Heidenhofstr. 2, 79110 Freiburg, Germany
andrea.pfreundt@ise.fraunhofer.de

ABSTRACT: We measure the thickness of the encapsulation layers in photovoltaic modules using scanning acoustic microscopy and optical microscopic imaging. Based on the measurement data, we analyze the impact of thickness variation on the operating temperature of the module, its peak power and mechanical stresses in the solar cells during lamination and under load testing conditions. Especially in cell-free areas we find an inhomogeneous thickness attributed to a bending of the backsheet, which has a small impact on the backsheet coupling gain. Even though we find significant deviation in the thicknesses of the encapsulation layer of up to 150 μm , the impact of encapsulant thickness under the investigated conditions is small and mainly attributed to changes in operating temperature.

Keywords: PV Module, Simulation, Encapsulation

1 INTRODUCTION

Developing new designs, materials and processes for photovoltaic modules generally involves prior simulations or calculations. Those theoretical investigations target the output power under various conditions, the annual yield [1][2], factors influencing its long term stability, such as the response to thermo-mechanical stresses [3], the processes in module production or the costs. Simulations are based on input parameters that are often idealized. The deviations between inputs and reality lead to an uncertainty in simulations.

The aim of this work is to investigate encapsulation thickness in photovoltaic modules after lamination. The work is based on measurement of the actual encapsulation thickness using two different methods. Scanning acoustic microscopy (SAM) is used as a first non-destructive method, optical microscopy of polished cross sections of the module as a second. Measurements are performed on a number of cross sections taken from different locations on the module. Implementing the resulting measurement values of layer thicknesses in different physical models, we analyze the impact of its variation on module performance parameters. We investigate module power under different irradiation conditions and ambient temperature using detailed models implemented in SmartCalc.CTM [4]. Stress in solar cells after lamination and under mechanical load conditions is modeled using finite element methods (FEM) [5,6].

2 EXPERIMENTAL

2.1 Preparation of test modules

Two 2x2-cell-modules and one 6x7-cell module are fabricated to investigate post-processing thicknesses of module layers. Cell-strings are fabricated from M2 sized (156.75 x 156.75 mm), monocrystalline silicon solar cells using a commercially available interconnecting ribbon (0.9 x 0.25 mm) and a Teamtechnik stringer TT1800. The strings are manually interconnected. Modules are laminated with ethylene vinyl acetate (EVA) and the material stack given in Table I using a membrane laboratory laminator from Meier (4-cell module) or an

industrial laminator from Bürkle (54-cell module) using established lamination processes.

Table I: Module stack materials

Layer no.	Material	Nominal thickness [mm]
1	Safety Glass	3.00
2	EVA	0.45
3	Solar cell	0.18 \pm 0.02
4	EVA	0.45
5	Backsheet	0.35

We use 3 mm low-iron thermally toughened glass for manufacturing. Cross sections are performed by cutting the glass at the positions as shown in Figure 1.

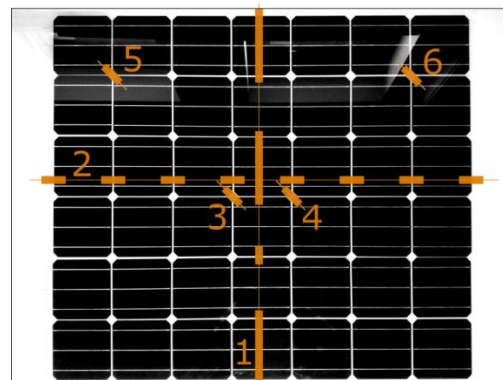


Figure 1: Location of the measurement locations / module cut-outs. 1 and 2 denote the full line of measurement across the module width and length, respectively.

2.2 Scanning acoustic microscopy (SAM) imaging

SAM is used to measure the thickness profiles in different positions of the full-size module. The locations on the module are shown in Figure 1. The module is immersed in water (19 °C) and the acoustic measurements are carried out at 15 MHz using a scanning acoustic microscope (PVA TePla Analytical Systems, SAM 500 HD²) in peak mode, lateral resolution of 70 μm /pixel. During the measurement, the amplitude of an ultrasonic probe signal is recorded as a function of the time-of-flight (TOF) for each pixel in a defined mapping

area. The recorded reflectograms show ultrasound reflections corresponding to interfaces between different materials (changes in sound speed / density). The pulse-echo signal is digitized at a sampling rate of 1.25 GSamples/s and the data stored in the internal hard drive for post-processing. A visual representation of the results, showing an averaged measurement parameter related to the depth of the first interface in gray scale, is shown in Figure 2. Off-line processing of the data is conducted with the MATLAB-based SAMANALYSIS software (PVA TePla Analytical Systems at Fraunhofer IWM, Halle, Germany). A reflectogram is collected at one point every 0.25 mm along a profile in the mapped area from which the thickness profiles are generated. The received signal is transformed using the Hilbert transform to obtain the signal envelope. The peak maxima in the Hilbert envelope are regarded as the material interfaces and their distances (measured in time units) are used to determine the layer thickness using known material parameters for EVA (density $\rho = 952 \text{ kg/m}^3$, coefficient of stiffness $C = 2500 \text{ MPa}$). The TOF differences are then converted into material thickness using the following relation:

$$d = \frac{\Delta TOF}{2} \sqrt{\frac{C}{\rho}}$$

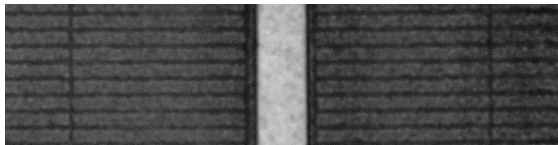


Figure 2: Acoustic micrograph of the cell gap.

2.3 Thickness measurement by optical microscopy

Module cut-outs are prepared in the same locations where SAM measurements are recorded to enable thickness measurement by optical microscopy. The cross sections are investigated with an optical digital microscope (Olympus DSX 510). Images are taken of the area between the backsheet and the front glass with a 5x objective, so that backsheet, encapsulation layers, cell and lower edge of the front glass are visible. Along the cut-line, measurements are taken every 250 μm , starting at 2.5 mm from the cell edge, across the cell gap and up to a distance of 2.5 mm on the cell on the opposite side (only one-sided for cut-out A). The uncertainty of the measurement is partly due to positioning of the measurement spot on the edges of the materials, and partly due to material roughness. Estimated from measurements of the cell thickness within each cut, which is assumed to be constant, the uncertainty of the thickness measurement is approximately $\pm 7 \mu\text{m}$.

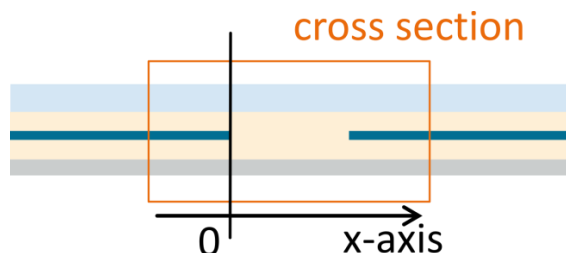


Figure 3: Schematic of the module cross section detailing the position of the x-axis along which measurements are taken.



Figure 4: Microscope image showing an example of a module cross section with a 3 mm cell gap.

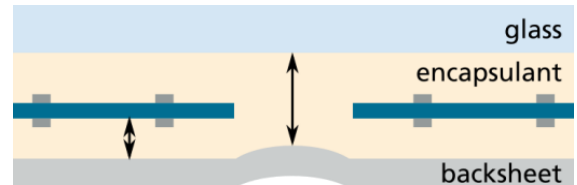


Figure 5: Schematic sketch of different encapsulation thicknesses within a PV module

3 MODELING

3.1 Optical and thermal losses and gains

Impacts of the variations in thickness are investigated using the models implemented in SmartCalc.CTM [4,7]. Relevant impact factors are shown in Figure 6. The thickness of the module layers directly impacts light absorption in the materials and has an impact on secondary coupling effects by both changes in absorption and the angular redistribution of light. A simplified ray tracing approach is used to investigate the effect of curvature in the backsheet on the coupling gain [7]. The cell temperature is modeled using a physical steady-state thermal model based on a one-dimensional layered module system [8]. The temperature dependence of the thermal conductivity and emissivity are neglected and values measured at 25°C are used. The parameters used in the model are listed in Table II.

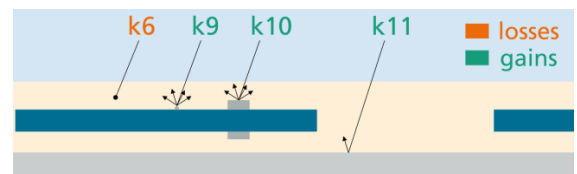


Figure 6: CTM loss and gain factors directly influenced by the encapsulation thickness.

Table II: Modeling parameters

Material	Thickness [mm]	Thermal conductivity [W/Km]	Emissivity
Glass	3.2	1	0.837
EVA	0.3 / 0.45	0.35	0.6
Solar cell	0.18	150	0.839
Backsheet	0.35	0.155	0.769

3.2 Modeling of the backsheet coupling gain at locations with inhomogeneous EVA thickness

The cell spacing and module border areas contribute to the module power by reflection of light at the visible backsheet area [7,9]. This gain depends on the optical properties of the module materials especially the reflectivity of the backsheet surface. Inhomogeneous

EVA thickness in this area means, that the backsheet is bent towards the module front leading to a curved surface reflecting the light. Several models for calculation of the backsheet coupling gain are unable to consider this effect and assume a flat backsheet surface [10,11]. We model the curved backsheet surface using and interpolation of the measured data as input of the curvature and investigate the impact on the coupling gain and module power for diffuse and partially specular reflecting backsheets.

3.3 FEM Modeling of mechanical stress in solar cells

To investigate the influence of the different EVA thicknesses on the stress in solar cells, we use a finite element method (FEM) simulation and perform a variation of the encapsulant thickness from 300 μm to 450 μm in 25 μm steps.

For this study two validated FEM models [5,6] are merged. The solar cells are implemented as full-square mono-crystalline silicon wafer, neglecting metallization and ribbons. We use hexahedral mesh elements with 2,700 mesh elements per solar cell and a quadratic serendipity basis function. The two-fold axial symmetry is utilized by modeling a quarter laminate. We use linear elastic and temperature dependent material models given in [5].

The FEM model covers lamination and mechanical load (ML). For ML we add an aluminum frame to the laminate. We simulate the mounting of the framed module on a rack by a fixed constraint on the long side of the module with a distance of 20% of the long side to its edge. We simulate the lamination process by cooling down from 150 $^{\circ}\text{C}$ to 25 $^{\circ}\text{C}$. Subsequently, we simulate a homogenous push load of 2400 Pa and 5400 Pa. The residual stress from lamination is considered in ML.

4 RESULTS AND DISCUSSION

4.1 Qualitative investigation of cell spacing and module border

The graphs in Figure 7 show the time of flight (TOF) plots obtained with the scanning acoustic microscope (SAM). Figure 7 a) shows the regular cell spacing of approximately 4 mm (2d), b) shows the diagonal across the pseudo-square corners of the cells (4) and c) shows the module border at the edge of profile 1c. Both a) and b) are obtained close to the center of the module. In each image three interfaces are easily distinguished: from top to bottom: air/backsheet, backsheet/encapsulant and encapsulant/cell or encapsulant/glass (module front cover). A bending of the backsheet is clearly visible in b) and c), while in a) only a small difference can be seen.

4.2 Encapsulation thickness variation across the module

From measurements performed on microscopic images of the prepared module cross sections we find a thickness variation in the encapsulation material EVA. The front and rear side encapsulation layer with a nominal pre-processing thickness of 450 μm shows a variation in thickness across the module. We measure the thickness above and below the cell close to the cell gaps in the positions indicated in Figure 1 on the full size module and fewer, but equally distributed measurement locations on the small modules (not shown). For the 2x2 module a minimum of $299 \pm 9 \mu\text{m}$ and a maximum EVA thickness of $370 \pm 9 \mu\text{m}$ are found after lamination, with

an average thickness of $347 \pm 12 \mu\text{m}$ and $341 \pm 21 \mu\text{m}$ in front and rear of the cells, respectively. For the 6x7 module we find a minimum thickness of $315 \pm 3 \mu\text{m}$ and a maximum of $393 \pm 6 \mu\text{m}$ with an average of $369 \pm 16 \mu\text{m}$ (front) and $365 \pm 19 \mu\text{m}$ (rear). The distribution of the measured EVA thickness shows no apparent trend in different sections of the modules and values appear to be randomly distributed. The measurements show that there is a significant deviation in thickness reduction between 13 and 33% compared to the nominal material thickness. In the following we consider the impact of a variation of the EVA thickness on different aspects of module performance.

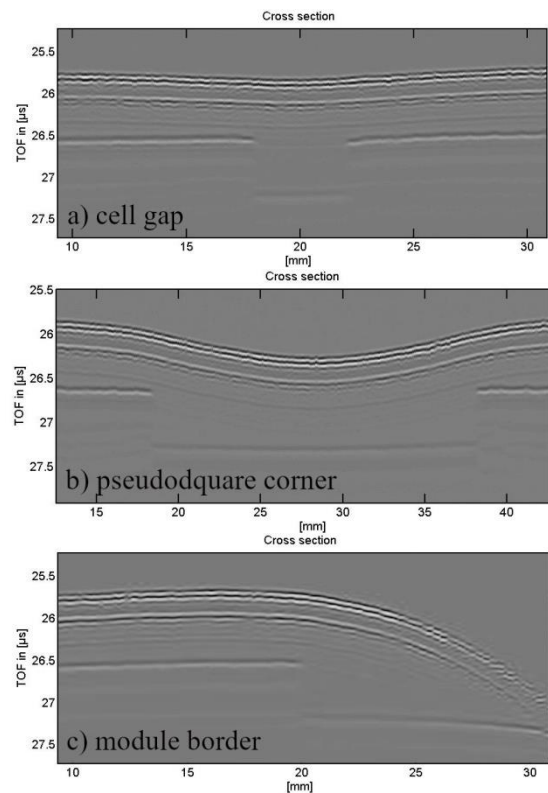


Figure 7: Raw SAM images showing the time of flight (TOF) on the y-axis, location on a profile line on the module on the x-axis and amplitude of the ultrasound signal in grayscale. Interfaces in the module materials are visible as multiple lines (reflected waves). Measurements are taken from the backside of the module, so the interface seen at the top of the image is the backsheet.

4.3 Backsheet bending in cell gaps

The thickness variation of the encapsulation layer at the cut line across the cell gaps and at the cell edges is measured. We find that for cell distances as small as 3 mm the thickness of the EVA stack gets thinner with increasing distance from the cell edges resulting in a small bending in the backsheet towards the module front (see schematic drawing in Figure 5). The larger the cell gap, the more pronounced the effect becomes. It is most pronounced at the module edge and in the pseudo-square cell corners, where the cell-free space is especially large. SAM images of the respective areas are shown in Figure 7. At the thinnest point, in the center of the pseudo-square corner area, the encapsulant thickness is reduced to 720 μm , in one case even down to 620 μm in the center of the module. The first corresponds roughly to the

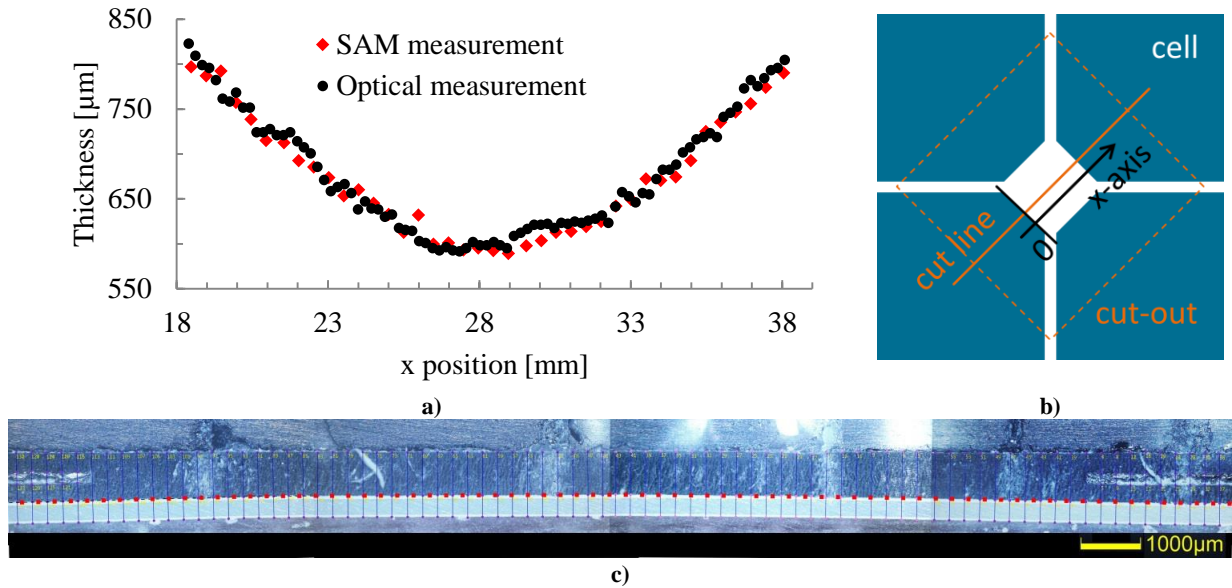


Figure 8: a) Measured thickness of the EVA layer using SAM and optical microscopy of polished cross sections. The measurement shows the pseudo-square cell corner in location 4 (see Figure 1). b) Schematic of the module section (top view) at the pseudo square edges. c) Stacked microscopic image showing the bending of the backsheet (images are aligned assuming no bending occurs in the glass).

sum of the encapsulant thicknesses found in the front and in the rear of the cells. In the cell gap we find a bending height between 25 and 65 μm.

Analysis of the backsheet coupling gain using a simplified raytracing method [7] shows the impact of the curved surface on module power gains. For the model, a parabolic curve was fitted to the measured data which we find to be a suitable description of the curved surface. For a fully diffuse reflecting backsheet the difference in coupling gain is mainly due to a change in absorption along the light path and has a very small impact on module power. We find a gain of less than 0.2 Wp for a rather large bend of 50 μm in the cell gap compared to the flat surface at 400 μm encapsulant thickness. For a uniform thickness reduction of 150 μm (300 μm compared to 450 μm) we find a 6% increase corresponding to up to 0.5 Wp at STC conditions.

We expect the impact of the bending on the module edge to be more significant in terms of backsheet coupling. But since the distribution will be inhomogeneous across the cells (only at the outer cells), mismatch effects on the module level will impact the overall module performance. Therefore the analysis of this effect is beyond the scope of this paper.

4.4 Comparison of predicted module power for different (uniform) EVA thicknesses

We calculated the influence of encapsulant thickness on module power using the cell-to-module analysis tool SmartCalc.CTM (version 1.2.1). We analyze a conventional monofacial glass/backsheet module setup and for comparison a bifacial glass/glass setup with 60 monocrystalline solar cells. The EVA thickness in front and back of the cell layer is varied between 300 μm and 450 μm. Module temperature and output power are calculated under different irradiation and ambient temperature conditions. We find a maximum deviation in module power of 1.2 W in the investigated range of thickness values and setup parameters (Table III).

Table III: Difference in module peak power for EVA thickness of 300 and 450 μm, $\Delta P_{MPP} = P(300\mu\text{m}) - P(450\mu\text{m})$ at 1000 W/m² irradiance.

ΔP_{MPP} [W]	glass / backsheet	glass / glass
0°C	1.21 W (0.44%)	0.79 W (0.28%)
15°C	1.15 W (0.44%)	0.78 W (0.28%)
30°C	1.15 W (0.48%)	0.74 W (0.30%)

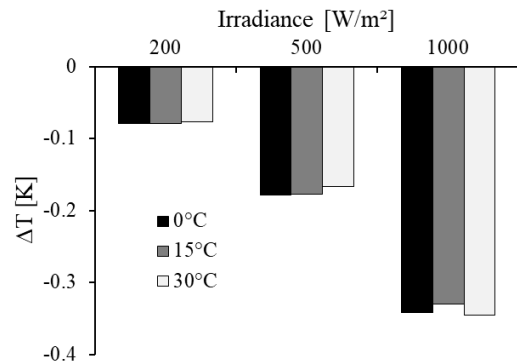


Figure 9: Temperature difference in monofacial modules with different thicknesses of the encapsulation layers. $\Delta T = T(300\mu\text{m}) - T(450\mu\text{m})$.

As expected due to decreasing optical losses, the thinner EVA yields a higher module power. However, the difference in optical absorption contributes only a third of the difference in power; 0.14% relative, with similar values for glass-backsheet and glass-glass modules. Additional thermal gains due to lower cell temperatures account for an additional increase in power of up to 0.17% for both module types, depending on the irradiance level. The remaining power difference and the considerable deviation between the two module types is attributed to changes in backsheet coupling; in this case only due to differences in thickness, neglecting the curvature of the surface. Figure 9 shows the difference in operating temperatures between modules that differ only in EVA thickness. The simulated cell temperatures for

each condition and for different thicknesses in EVA are listed in Table IV.

Table IV: Module temperatures for selected module setups for 450 μm EVA thickness.

T [°C]	glass / backsheets			glass / glass		
	Irradiance [W/m ²]					
Amb. T	200	500	1000	200	500	1000
0°C	10.2	27.7	52.9	10.3	27.9	53.2
15°C	24.7	41.8	66.3	24.8	42.0	66.7
30°C	39.9	56.2	79.8	39.9	56.3	80.2

4.5 Stress in solar cells

We analyze the impact of different EVA thicknesses on mechanical stress and the related probability of failure in solar cells. The thickness is assumed to be uniform across the module. Figure 10 shows the minimum third principal stress σ_{III} , which is the compressive stress equivalent, of the solar cells after lamination. The compressive stress decreases for an increasing encapsulant thickness, because the mismatch of the coefficient of thermal expansion between the solar cells and the front glass as well as the backsheets is more compensated for a thicker EVA.

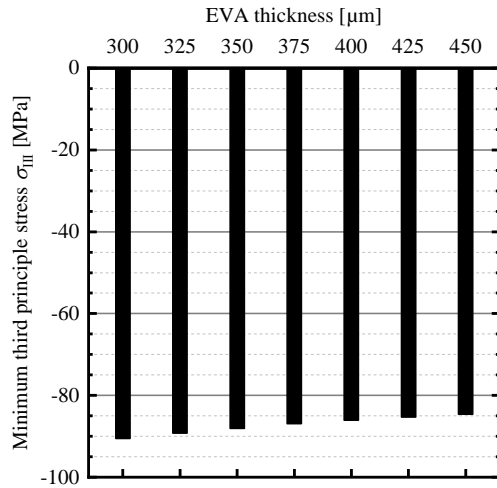


Figure 10: Minimal third principal stress σ_{III} in the solar cells after lamination for different EVA thicknesses.

Figure 11 shows the maximum first principal stress σ_I , which is the tensile stress equivalent, of the solar cells at a push load of 2400 Pa and 5400 Pa. Due to its softness, the EVA relaxes the stress in the solar cells. This relaxation effect increases with increasing EVA thickness. On the other hand, the compressive stress from lamination, which compensates the tensile stress partially, decreases with increasing EVA thickness for the same reason. Therefore, the tensile stress at 2400 Pa decreases minimally with increasing EVA thickness. At 5400 Pa, the tensile stress is higher, hence, the influence of the compressive stress from lamination becomes less and the decrease in tensile stress from 300 μm to 450 μm becomes more significant.

As a brittle material, silicon solar cells fail under tensile stress, thus the tensile stress is converted into a probability of failure $P(\sigma)$, using the Weibull distribution [12] considering the size effect with values from Kaule *et al.* [13], which is described in more detail elsewhere [14]. The probability of failure P_f gives the probability that

at least one crack is formed in at least one solar cell within the whole module. At 2400 Pa all stresses correspond to negligible probabilities of failure. At 5400 Pa the values become more critical with values between 81% (300 μm) and 67% (450 μm).

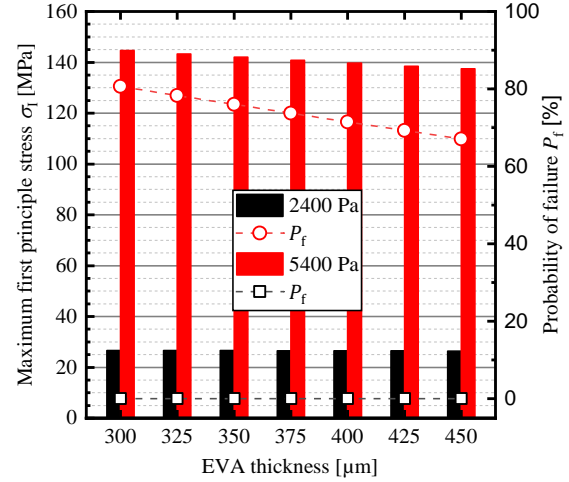


Figure 11: Maximum first principle stress σ_I in the cells during simulation of 2400 Pa and 5400 Pa load test for different EVA thicknesses with the corresponding probability of failure.

5 CONCLUSION

We find significant deviations between the nominal EVA thickness of pre-processed sheets and encapsulant layer thickness after lamination in photovoltaic modules from 150 μm to 50 μm . In different locations of the investigated module we find a non-uniform distribution of thicknesses especially in the cell gaps and at the edge of the module. We analyze the impact of thickness variations on module performance and find deviations in module power attributed to changes in operation temperatures. As expected, thinner EVA layers lead to a higher failure probability of the solar cells as shown by a mechanical load test simulation. Overall we find that even though the measurements deviate significantly from nominal values, for the investigated cases the thickness variation has a very small impact on module performance and the failure probability in mechanical load tests.

The impact of inhomogeneous EVA thicknesses across different parts of the module on operation temperature and mechanical stress has not been investigated here and will be the focus of further work.

6 ACKNOWLEDGEMENT

We would like to thank the German Federal Ministry of Economic Affairs and Energy (FKZ 0324289A) for their funding.

REFERENCES

- [1] I. Hädrich, U. Eitner, M. Wiese, H. Wirth, Sol Energ Mat Sol C 131 (2014), 14–23.
- [2] M. Mittag, T. Zech, M. Wiese, D. Blaesi, M. Ebert, H. Wirth, in: 44th IEEE PV Specialist Conference PVSC.

- [3] A.J. Beinert, P. Romer, A. Büchler, V. Haueisen, J. Aktaa, U. Eitner, *Energy Procedia* 124 (2017), 464–469.
- [4] Fraunhofer Institute for Solar Energy Systems ISE SmartCalc.CTM.
- [5] A.J. Beinert, A. Büchler, P. Romer, M. Heinrich, M.C. Schubert, J. Aktaa, U. Eitner, *Proceedings of the 7th World Conference on Photovoltaic Energy Conversion* (2018), 3613–3617.
- [6] A.J. Beinert, R. Leidl, P. Sommeling, U. Eitner, J. Aktaa, in: *33rd European Photovoltaic Solar Energy Conference and Exhibition (EUPVSEC) 2017*, pp. 42–47.
- [7] A. Pfreundt, M. Mittag, M. Heinrich, U. Eitner, *32nd European Photovoltaic Solar Energy Conference and Exhibition (EUPVSEC) (2018)*.
- [8] M. Mittag, L. Vogt, C. Herzog, D.H. Neuhaus, in: *36th European Photovoltaic Solar Energy Conference and Exhibition (EUPVSEC) 2019*.
- [9] M. Mittag, A. Grünzweig, M. Wiese, N. Mahmoud, A. Schmid, M. Heinrich, *33rd European PV Solar Energy Conference and Exhibition 2017*.
- [10] J.P. Singh, S. Guo, I.M. Peters, A.G. Aberle, T.M. Walsh, *IEEE J. Photovoltaics* 5 (2015), 783–791.
- [11] O. Dupré, J. Levrat, J. Champlaud, M. Despeisse, M. Boccard, C. Ballif, in: *Silicon PV 2018*, p. 90001.
- [12] W. Weibull *A Statistical Theory of the Strength of Materials*, Generalstabens Litografiska Anstalts Förlag, Stockholm (1939).
- [13] F. Kaule, M. Pander, M. Turek, M. Grimm, E. Hofmueller, S. Schoenfelder, *SiliconPV 2018, The 8th International Conference on Crystalline Silicon Photovoltaics: Conference date, 19-21 March 2018 location, Lausanne, Switzerland (2018)*, 20013.
- [14] A.J. Beinert, P. Romer, M. Heinrich, M. Mittag, J. Aktaa, H. Neuhaus, *Proceedings of the 36th European Photovoltaic Solar Energy Conference and Exhibition (2019)*.